Ligthill's aeroacoustic Analogy applied to an automotive turbocharger compressor

Clemens Freidhager[1], Stefan Schoder[1], Andreas Renz[2], Martin Heinisch[3], Manfred Kaltenbacher[1]
[1] *IGTE, University of Technology Graz, 8010 Graz, Austria, Email: clemens.freidhager@tugraz.at*
[2] *iPAT, Universität Erlangen-Nürnberg, 91058 Erlangen, Germany*
[3] *BMW Motoren GmbH Steyr, 4400 Steyr, Austria*

Introduction

One possible way of reducing CO_2 emissions while still using internal combustion engines is by applying a turbocharger. Turbochargers may increase the specific power output of a combustion engine and therefore allows downsizing while keeping the engine power constant [1, 2]. Since further law and regulations were passed in the European Union limiting the noise from cars driven by a combustion engine [3], turbocharger acoustics shifted into focus.

Following, turbocharger compressor is investigated as studies have shown that it is the main source of turbocharger noise [2]. Acoustics of turbocharger compressor have already been investigated in detail using compressible, transient flow simulations [4, 5, 6, 7, 8, 9]. In contrast, we focus on Lighthill's aeroacoustic analogy for computing pressure propagation based on the Finite Element (FE) method. Using Lighthill's analogy brings up the advantage that the flow and pressure propagation can be computed on different grids, both designed for their specific purpose. Furthermore, the flow computation can be limited to a small area in which significant turbulent eddies and therefore aeroacoustic source terms are expected. In addition, computing pressure fluctuation using a linear wave operator in combination with the FE method is less influenced by numerical dissipation effects, like flow solvers based on Finite Volumes (FV).

For applying Lighthill's analogy the hybrid aeroacoustic workflow, [10, 11, 12, 13], is applied (see Fig. 1) [14]. Following it's four main steps are discussed:

1. A transient, compressible CFD simulation is performed. In parallel Lighthill's source terms are computed.
2. The computed source terms are interpolated from the CFD to the propagation grid.
3. The mean value of the source terms is eliminated by applying a Fast Fourier Transformation (FFT), neglecting the mean value, and applying an Inverse Fast Fourier Transformation (iFFT).
4. Finally, the propagation simulation is performed.

For evaluation purposes, measurements established on a cold gas test rig (CGTR) for two different evaluation points in the compressor inlet (see Fig. 2) are used. The cold gas test rig is located inside of an acoustic chamber and is specially designed for measuring in-duct pressure fluctuations and acoustic pressure fluctuations outside of

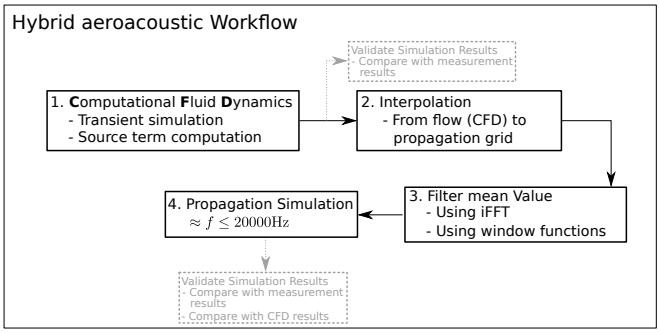

Figure 1: Main steps of the hybrid aeroacoustic workflow used for computing pressure propagation in the turbocharger compressor.

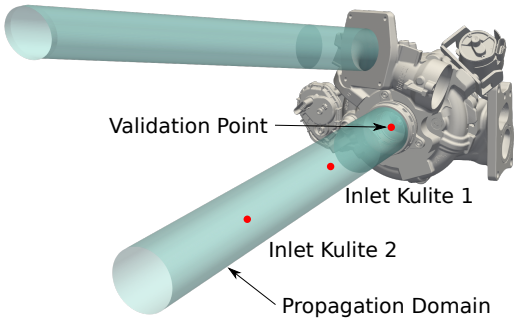

Figure 2: Propagation domain with the two evaluation points.

the turbocharger compressor. For more details, we refer to [15]. For both of those two evaluations points, CFD and propagation simulation results are compared with measurements.

Finite Element Formulation of Lighthill's Equation

Lighthill's aeroacoustic analogy was presented in 1952 and 1954 by M.J. Lighthill [16, 17]. For the following finite element formulation we consider Lighthill's inhomogeneous wave equation

$$\left(\frac{1}{c_0^2}\frac{\partial^2}{\partial t^2} - \Delta\right) c_0^2(\rho - \rho_0) = \nabla \cdot \nabla \cdot [\boldsymbol{T}]\,, \qquad (1)$$

with c_0 as the ambient speed of sound, Δ as Laplace operator, ρ as density, and $[\boldsymbol{T}]$ as Lighthill's stress tensor. Lighthill's equation is a direct reformulation of the compressible flow equations without any simplifications. As a result, solving Lighthill's equation requires corresponding boundary conditions for the propagation

simulation, which represent the boundary conditions used in the CFD simulation. The expected ideal propagation results using Lighthill's analogy in combination with the FE method are equal to the CFD simulation results. However, if CFD and propagation domains do not fully align, there will be differences between the two results. Consequently, if the propagation simulation is performed for a very different propagation domain, the source terms represent a flow from the original flow domain, and the computed results will differ.

In the next step, the FE method is applied to Lighthill's inhomogeneous wave equation (1). Therefore, we multiply the partial differential equation with a test function φ and integrate over the computational propagation domain Ω

$$\int_\Omega \left(\frac{1}{c_0^2}\frac{\partial^2}{\partial t^2} + \Delta\right)(c_0^2(\rho-\rho_0))\varphi - (\nabla\cdot\nabla\cdot[\boldsymbol{T}])\varphi \,\mathrm{d}\Omega = 0\,. \tag{2}$$

Now, integration by parts is applied to the Laplace term of the differential operator and to the right-hand side, bringing up

$$\begin{aligned}\frac{1}{c_0^2}\int_\Omega \varphi\frac{\partial^2}{\partial t^2}c_0^2(\rho-\rho_0)\mathrm{d}\Omega + \int_\Omega \nabla c_0^2(\rho-\rho_0)\cdot\nabla\varphi\mathrm{d}\Omega \\ - \int_\Gamma \nabla c_0^2(\rho-\rho_0)\cdot\boldsymbol{n}\varphi\Gamma = \\ - \int_\Omega \nabla\cdot[\boldsymbol{T}]\cdot\nabla\varphi\mathrm{d}\Omega + \int_\Gamma \nabla\cdot[\boldsymbol{T}]\cdot\boldsymbol{n}\varphi\mathrm{d}\Gamma\,.\end{aligned} \tag{3}$$

Finally, corresponding boundary conditions as presented in [18] are applied, bringing up the following final weak formulation

$$\begin{aligned}\frac{1}{c_0^2}\int_\Omega \varphi\frac{\partial^2}{\partial t^2}c_0^2(\rho-\rho_0)\mathrm{d}\Omega + \int_\Omega \nabla c_0^2(\rho-\rho_0)\cdot\nabla\varphi\mathrm{d}\Omega = \\ - \int_\Omega \nabla\cdot[\boldsymbol{T}]\cdot\nabla\varphi\mathrm{d}\Omega + \int_{\Gamma_\mathrm{I}} (\nabla\cdot[\boldsymbol{T}] + \nabla c_0^2(\rho-\rho_0))\cdot\boldsymbol{n}\varphi\mathrm{d}\Gamma\,.\end{aligned} \tag{4}$$

Results

For modeling the transient, and turbulent flow inside of the compressor an Improved Delayed Detached Eddy Simulation (IDDES) with an underlying k-ω SST turbulence model implemented in StarCCM+ [19] was used. Further, a segregated flow solver with a hybrid second-order upwind/bounded-central scheme for convection was used. For rotating the impeller region, a rigid body rotation was applied. Furthermore, a mass flow inlet and a pressure outlet boundary condition were used. For mesh generation, polyhedral cells, with refinements at regions with high-velocity gradients, were used. A base grid size of 1.6 mm in the inlet and outlet region, as well as 1.3 mm in the impeller region, was used. In the inlet and outlet region, 10 prism layers with an overall thickness of 0.8 mm and a growing ratio of 1.05 were applied. In the wheel region, 10 to 18 prism layers were used, with the highest number of prism layers located at the blade surfaces. This leads to the number of 30 cells in the blade tip gap. Finally, the CFD mesh consists of 22 446 702 cells. Furthermore, a time step corresponding to 1° of rotation of the impeller was considered and a second-order, implicit time-stepping scheme was applied.

For the propagation simulation, the source terms are interpolated from the CFD mesh onto the propagation grid using the Least Square mapping algorithm implemented into StarCCM+ [19]. For generating the propagation grid, tetrahedral elements with a base size of 1.7 mm are used. The element size of the propagation grid orientates on the highest frequency that has to be resolved, which in this case is 20 kHz. Thereby, the corresponding wavelength has to be approximated by at least ten elements. Due to the established weak formulation (see. (4)) it is possible to limit the propagation domain, cutting out any region (see Fig. 3). Thereby, the neglected regions are incorporated by applying an interface boundary condition, as shown in the last term of (4). Consequently, in this paper, we limit the simulation to the compressor inlet. This allows us to cancel out the rotating impeller and enables us to perform the propagation simulations using much smaller propagation domains, hence making the simulation faster. Furthermore, a Perfectly Matched Layer (PML) is applied for simulating the open end of the pipe (see Fig. 3). Ultimately this leads to 2 911 950 cells in the inlet propagation domain. By solving the presented weak formulation density fluctuations

$$\rho' = \rho - \rho_0\,, \tag{5}$$

are computed. To convert the density in a pressure fluctuation local speed of sound is considered

$$p' = c^2\rho'\,. \tag{6}$$

For the propagation simulation our in-house openSource multi-physics Finite Element Solver openCFS [20] was used.

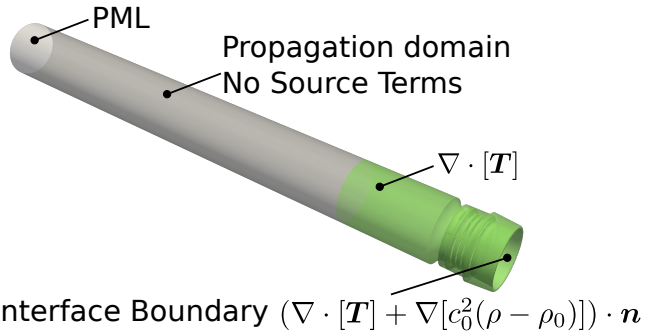

Figure 3: Propagation domain of the inlet with interface boundary condition. In the green part of the domain source terms are considered. At the open duct end a PML is applied.

First, an evaluation point located inside of the source term domain (see Fig. 2 & 3), is investigated. Since this evaluation point is located very close to the impeller (about 0.005 mm away from the impeller hub), no

measurements could be performed for this point. However, comparing the CFD and pressure propagation results (see Fig. 4) shows good agreement, validating the general functionality of the approach. The difference between the two simulation results can be connected with differences in the flow and propagation domains Finally,

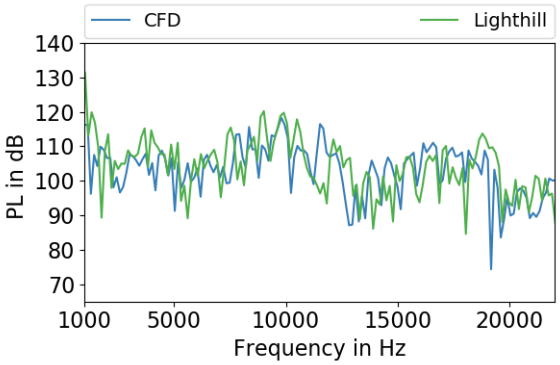

Figure 4: Simulation results of the validation point (see Fig. 2) of the CFD and the Lighthill propagation simulation of 10 turns with n=88740 rpm. For both signals a hamming window function was applied.

comparing measurements with CFD and pressure propagation results (see Fig. 5 & 6) at the two evaluation points shows respectively good agreement. Differences between both simulation and measurements results are because measurement signals with 30 s of data, and simulations with 0.00676 s of data (which corresponds to 10 turns) were used. In addition, comparing the results of the CFD and the pressure propagation simulation shows that the CFD simulation results are affected by numeric dissipation, especially at Inlet Kulite 2.

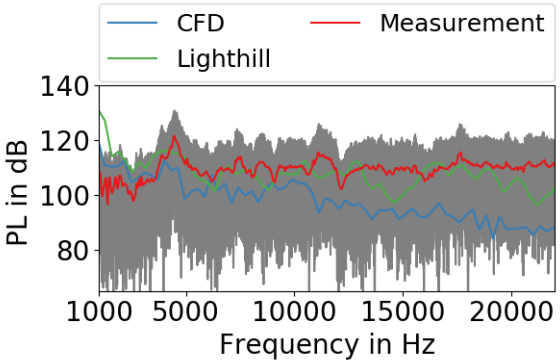

Figure 5: Simulation results and measurements of *Inlet Kulite 1*. For post-processing, the 30s of the measurement were split into 500 blocks with 0.2 overlap. The spectrum of every single block of the measurement is depicted in grey. The CFD and Lighthill propagation simulation result of 10 turns with n=88740 rpm were split into 3 blocks with 0.2 overlap. For all simulation results, a hamming window function was applied.

Conclusion

We could show that Lighthill's inhomogeneous wave equation used in combination with the Finite Element

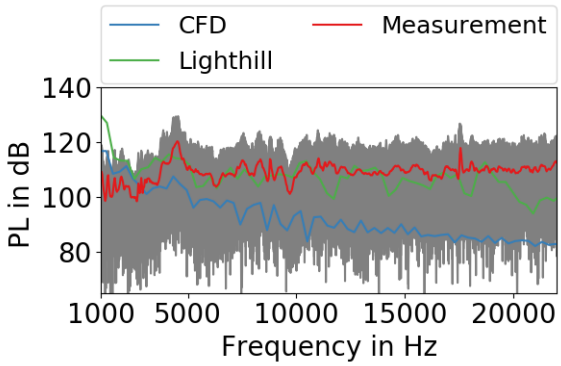

Figure 6: Simulation results and measurements of *Inlet Kulite 2*. For post-processing, the 30s of the measurement were split into 500 blocks with 0.2 overlap. The spectrum of every single block of the measurement is depicted in grey. The CFD and Lighthill propagation simulation result of 10 turns with n=88740 rpm were split into 3 blocks with 0.2 overlap. For all simulation results, a hamming window function was applied.

Method is able of computing pressure fluctuations based on a compressible CFD simulation. Furthermore, it could be shown that CFD simulation results are affected by numeric dissipation, whereas the pressure propagation does not show up numeric dissipation.

Acknowledgments

This research was funded by a bridge project (project number 867971) of the Austrian Research Promotion Agency (FFG).

References

[1] Golloch, R. *Downsizing bei Verbrennungsmotoren*. Springer, 2005.

[2] Nguyen-Schäfer, H. *Aero and Vibroacoustics of Automotive Turbochargers*. Springer, 2013.

[3] European Parliament. On the sound level of motor vehicles and of replacement silencing systems, and amending. Technical report, European Parliament, november 2020. `https://eur-lex.europa.eu/legal-content/EN/TXT/?uri=CELEX:32014R0540`.

[4] Broatch, A. Galindo, J. Navarro, R. Garcia-Tiscar, J. Methodology for experimental validation of a CFD model for predicting noise generation in centrifugal compressors. *International Journal of Heat and Fluid Flow*, 2014.

[5] Broatch, A. Galindo, J. Navarro, R. Garcia-Tiscar, J. Simulations and measurements of automotive turbocharger compressor whoosh noise. *Engineering Applications of Computational Fluid Mechanics*, 9(1), 2015.

[6] Fontanesi, S. Paltrinieri, S. and Cantore, G. CFD analysis of the acoustic behavior of a centrifugal compressor for high performance engine application. *Energy Procedia*, 45, 2014.

[7] Semlitsch, B. and Jyothishkumar, V. and Mihaescu, M. and Fuchs, L. and Gutmark, E. J. Investigation of the surghe phenomena in a centrifugal compressor using large eddy simulation. *Proceedings ASME 2013*, 2013.

[8] Mendonça, F. Baris, O. Capon, G. Simulation of a radial compressor aeroacoustics using CFD. *Proceedings of ASME Turbo Expo*, 44748:1823–1832, 2012.

[9] Sundström, E. Flow instabilities in centrifugal compressors at low mass flow rate. *KTH Mechanics, Royal Institute of Technology. Stockholm, Sweden*, 2017. PhD Thesis.

[10] Stefan Schoder, Klaus Roppert, Michael Weitz, Clemens Junger, and Manfred Kaltenbacher. Aeroacoustic source term computation based on radial basis functions. *International journal for numerical methods in engineering*, 121(9):2051–2067, 2020.

[11] Stefan Schoder, Andreas Wurzinger, Clemens Junger, Michael Weitz, Clemens Freidhager, Klaus Roppert, and Manfred Kaltenbacher. Application limits of conservative source interpolation methods using a low mach number hybrid aeroacoustic workflow. *Journal of Theoretical and Computational Acoustics*, 2021.

[12] Stefan Schoder, Clemens Junger, Michael Weitz, and Manfred Kaltenbacher. Conservative source term interpolation for hybrid aeroacoustic computations. In *25th AIAA/CEAS Aeroacoustics Conference*, page 2538, 2019.

[13] Stefan Schoder, Clemens Junger, and Manfred Kaltenbacher. Computational aeroacoustics of the eaa benchmark case of an axial fan. *Acta Acustica*, 4(5):22, 2020.

[14] Clemens Freidhager, Paul Maurerlehner, Klaus Roppert, Andreas Wurzinger, Alexander Hauser, Martin Heinisch, Stefan Schoder, and Manfred Kaltenbacher. Simulationen von strömungsakustik in rotierenden bauteilen zur entwicklung von antriebskonzepten der autos der zukunft. *e & i Elektrotechnik und Informationstechnik*, pages 1–7, 2021.

[15] Johannes Klaus Müller. *Zur Schallabstrahlung des Abgasturboladers in Abhängigkeit der Verdichter- und Turbinenanströmung*. PhD thesis, 2020.

[16] M. J. Lighthill. On sound generated aerodynamically. i. general theory. *Proceedings of the royal society*, 1952.

[17] M. J. Lighthill. On sound generated aerodynamically. ii. turbulence as a source of sound. *Proceedings of the royal society*, 1954.

[18] Max Escobar. *Finite Element Simulation of Flow-Induced Noise using Lighthill?s Acoustic Analogy*. PhD thesis, 2007.

[19] Siemens. Star-ccm+ v. 12.06.

[20] openCFS. Finite elements for computational multiphysics v. 18.03; www.opencfs.org.